UC Berkeley
UC Berkeley Previously Published Works

Title

XtalCAMP: a comprehensive program for the analysis and visualization of scanning Laue X-ray micro-/nanodiffraction data

Permalink

Journal

ISSN

Authors

Li, Yao
Chen, Kai
Dang, Xiaofeng
et al.

Publication Date

DOI

Peer reviewed

111Equation Chapter 1 Section 1XtalCAMP: a comprehensive software for the analysis and visualization of scanning Laue X-ray micro/nano-diffraction data

Yao Li[a,b], Kai Chen[b]*, Fengying, Zhang[a], Nobumichi Tamura[c], Ching-Shun Ku[d], Hans-Rudolf Wenk[e]

[a]School of Materials Science and Engineering, Chang'an University, Xi'an, Shaanxi 710064, P.R. China

[b]Center for Advancing Materials Performance from the Nanoscale (CAMP-Nano), State Key Laboratory for Mechanical Behavior of Materials, Xi'an Jiaotong University, Xi'an, Shaanxi 710049, P.R. China. ***Correspondence Email: kchenlbl@gmail.com**

[c]Advanced Light Source, Lawrence Berkeley National Laboratory, Berkeley, CA 94720, USA

[d]National Synchrotron Radiation Research Center, Hsinchu, Taiwan 30076, R.O. China

[e]Department of Earth and Planetary Science, University of California, Berkeley, CA 94720, USA

bstract

XtalCAMP is a software package based on Matlab platform, which is ~~competent~~ adequate for, but not limited to, the analysis and visualization of ~~the~~ scanning Laue X-ray micro/nano-diffraction data. The main objective of the software is to provide complementary functionalities ~~for~~ to the current Laue indexation software packages ~~prevailing among~~ used at ~~different~~ several synchrotron beamlines. The graphical user interfaces allow the easy analysis of characteristic microstructure features, including real-time intensity mapping for a quick look of phase, grain and defects distribution, 2D color-coded mapping of microstructural properties ~~in~~ from the outputs of other Laue indexation software, grain boundary characterization based on orientation/misorientation calculation, principal strain/stress analysis and strain ellipsoid representation, as well as a series of additional toolkits. As an example, XtalCAMP is applied to the microstructural investigation ~~on~~ of a solution heat treated Ni-based superalloy manufactured using laser 3D-printing technique.

eywords: Scanning Laue X-ray micro/nano-diffraction, computer program, crystal orientation map, strain/stress analysis

1. Introduction

Taking advantage of brilliant synchrotron sources, the scanning Laue X-ray

micro/nano-diffraction (μXRD) technique has ~~been~~ become an indispensable high-throughput approach ~~to the linkage between~~for linking multi-scale microstructures ~~and~~ to physical properties in ~~a large area statistics~~statistically large areas of samples with excellent spatial (as good as tens of nm) and angular resolutions (~0.001°) (Chen *et al.*, 2016; Zhou *et al.*, 2018). With the μXRD technique, ~~a raster scan on the specimen~~the specimen is raster scanned under ~~by the~~a focused polychromatic X-ray beam and the diffraction ~~beams~~patterns at each scan spot are recorded using a 2D detector (i.e. Laue pattern) with a short exposure time (< 0.5 s). ~~Then the~~The spatial distributions of phases, crystal orientation, elastic strains/stresses and microstructural defects ~~are~~can then be extracted after analyzing the Laue patterns. Consequently, data analysis software, which is capable of indexing thousands of diffraction patterns automatically, has been a major necessity for the popularization of the μXRD technique.

Previous computer programs, such as LAUEGEN (Campbell, 1995), LaueX (Soyer, 1996) and OrientExpress (Ouladdiaf *et al.*, 2006), have been designed for Laue diffraction data analysis~~, while they aim~~ but aimed at isolated Laue pattern (LP) indexation and crystal orientation determination. This brings forth the development of in-house software at synchrotron beamlines to sequentially analyze thousands of LPs, ~~including~~ such as the X-Ray Microdiffraction Analysis Software (XMAS) (Tamura, 2014) at beamline 12.3.2 of Advanced Light Source (ALS) and ~~also applied at~~ beamline 21A of Taiwan Photon Source (TPS), LaueGo (Tischler) at beamline 34-ID-E of Advanced Photon Source (APS) and LaueTools (Micha, 2017) at the CEA-CNRS BM32 beamline of European Synchrotron Research Facility (ESRF). Although structured into different computer formats, the core outputs of these software packages are similar, comprising a matrix of the same dimension and size ~~of the scanning steps~~than the performed scan. Each element of the matrix ~~contain~~contains the crystal and microstructural information obtained from the analysis of the corresponding LP, for example the local crystal orientation, strain/stress tensor, LP background intensity, diffraction peak number and shape, and so on. The crystal orientation is usually expressed ~~by~~ in one or several of the following ways: ~~such as~~ orientation matrix, Euler angles, Rodrigues' rotation axis/angle pair and quaternions. The background intensity is an average value of all pixels on the 2D LP. The average full width at half maximum (FWHM) of all indexed Laue peaks in the angular space is taken to describe the diffraction peak shape. With these powerful software packages,

72 μXRD has been applied ~~into~~ to the investigation of phase identification and
73 structural evolution of micro/nano-crystals (Guo *et al.*, 2011; Strelcov *et al.*,
74 2012; Dejoie *et al.*, 2014), orientation mapping of single- or poly-crystalline
75 materials (Chen *et al.*, 2010; Ma *et al.*, 2015), transient and residual strain/stress
76 measurement in engineering and natural materials (Chen *et al.*, 2009, 2015; Li *et*
77 *al.*, 2018; Chen *et al.*, 2020), and defect density mapping (Lupinacci *et al.*, 2015;
78 Li *et al.*, 2018). In these typical applications of the μXRD technique, it is found
79 that the functionalities, such as 2D map plotting, misorientation computing, grain
80 boundary characterization and strain/stress distribution visualization, need to be
81 further explored and enhanced for general users.

82   Therefore, we introduce a custom-developed comprehensive software,
83 Crystal Computing and Mapping Program (XtalCAMP), ~~~~for the in-depth analysis
84 of the outputs of ~~the~~ μXRD data indexation, which incorporates a variety of easy-
85 to-use features including diffraction intensity study, basic 2D map plotting,
86 crystal orientation and misorientation analysis, grain boundary characterization,
87 strain/stress distribution visualization and other useful tools. As mentioned
88 above, the core information generated from indexation software packages such
89 as XMAS, LaueGo, and LaueTools is essentially the same; thereby we take the
90 XMAS outputs as the example in this article for the convenience of statement.

91 **2. Technical description, availability and requirements**

92   XtalCAMP is coded ~~based on~~through the MATLAB graphical user interface
93 (GUI) module ~~in Matlab~~ and can be executed on ~~Matlab~~ MATLAB R2014b ~~or~~and
94 higher versions installed on Windows 7 and 10 operating systems (32 bit or 64
95 bit). It has been registered at the Copyright Protection Centre of China
96 (Registration No. 2016SR060878).

97 **3. Program functionality and features**

98   The ~~primary~~ general architecture and principal functions of XtalCAMP are
99 ~~designed as~~ shown in Fig. 1. First of all, the diffraction intensity can be ~~calculated~~
100 extracted and mapped for qualitative microstructure imaging ~~without any assist~~
101 independently ~~of~~ from XMAS or any other LP indexation/analysis software.
102 Secondly, the outputs of ~~the~~ LP indexation software packages ~~, in the~~
103 ~~general~~(either in ASCII ~~formats~~ (*.txt) or specific binary *.seq formats generated
104 by XMA~~S)~~S, can be ~~inputted~~ directly imported into into XtalCAMP~~, and then~~
105 ~~2D~~2D maps can then be plotted for microstructure imaging ~~with~~ using various

3

106 ~~color styles~~colorbars and user defined threshold filters. Thirdly, further data
107 mining can be ~~carried out~~performed, including the plot~~ting~~ of pole figures,
108 inverse pole figures, ordinary grain boundaries, twin boundaries, misorientation
109 distributions, and so on. Finally, some of the toolkits ~~are~~ have easy-to-use
110 ~~developed with easy to use user interface~~user-friendly interface.
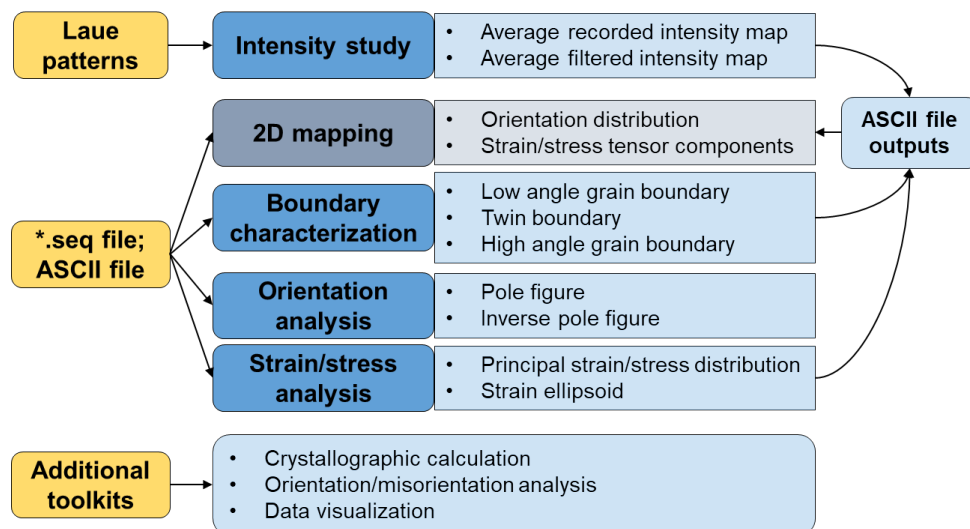
Figure 1 The architecture of XtalCAMP.

113 To ~~elucidate readily~~demonstrate the basic data processing functions of
114 XtalCAMP, a µXRD study of a heat treated DZ125L Ni-based superalloy
115 manufactured by laser 3D-printing is adopted as an example. A precipitation
116 hardened superalloy fabricated by directional solidification was selected as the
117 substrate. ~~There are mainly three kinds of phases containing in this alloy~~Three
118 kind of phases exist in this alloy:~~, that is,~~ γ austenite matrix, $L1_2$ ordered γ'-
119 Ni_3(Al, Ti, Ta) precipitates and MC-type carbides. Powders of the same
120 compositions ~~with~~ than the substrate were laser cladded on the (001) plane of
121 substrate. With the aid of high thermal gradient antiparallel to the building
122 direction, columnar grains ~~in the~~with width of ~500 µm grew in epitaxy with the
123 bottom substrate, extending to multiple cladding layers. Due to ~~the dense~~high
124 dislocation densitie~~s~~ and ~~high~~ residual strain/stress, complete recrystallization
125 occurred in the heat affected zone (HAZ) after post-manufacturing solution heat
126 treatment at 1240 °C for 2 h. ~~Then the~~The µXRD experiment was carried out at
127 ~~ALS~~ the ALS on beamline 12.3.2 (Kunz *et al.*, 2009). An ~~area of~~ 570 × 300 µm²
128 area on the longitudinal section of the ~~heat treated~~heat-treated sample was
129 raster scanned using the micro-focused X-ray beam with 3 µm step size,
130 covering ~~from~~ the substrate ~~to~~ and the cladding layers. Finally, ~~the~~a total 19000
131 LPs were automatically indexed using XMAS taking advantage of the newly

132 developed peak position comparison (PPC) indexing algorithm (Kou *et al.*, 2018)
133 and the indexation outputs were imported into XtalCAMP for further analysis. It
134 should be noted that all LPs were indexed ~~by~~ using the crystal structure of nickel,
135 due to the small misfit and cube-on-cube orientation relationship between γ and
136 γ′ phases (Li *et al.*, 2018). The detailed sample preparation and μXRD
137 experiment are described in Appendix A.

3.1. Diffraction intensity analysis and mapping

139 As indexing thousands of Laue patterns in a scan is time-consuming, we
140 developed a novel approach to collect the intensity of each LP without
141 indexation, facilitating a quick view of the characteristic microstructure features,
142 including cracks, voids, dendrite structures, precipitates, grain boundaries in a
143 real-time manner. The following lists the main steps of this approach:

144 (1) Read a LP and get the dimensions ($n \times m$ pixels) and ~~gray~~grey value
145 array. For the ith Laue pattern, the summation of ~~the gray~~the grey values ~~of~~from all
146 pixels is averaged~~, which~~. This is called average recorded intensity I_R of ith LP and
147 is defined as:

$$I_R = \frac{\sum_{k=1}^{n \times m} I_r^k}{n \times m}$$

148   22* MERGEFORMAT ()

149 where the I_r^k is the ~~gray~~grey value of kth pixel.

150 (2) To enhance the microstructural contrast, treatment is required to
151 distinguish the LPs with different peak shape. The approach adopted here is to
152 set a threshold intensity (I_t) for each LP, which is defined as $I_t = C_f \cdot I_R$. C_f is the
153 filter~~ed~~ factor, which is ~~a~~ constant for all the LPs taken in the whole scanned
154 area, and by default C_f is ~~take as~~equal to 4. The detailed reason why this method
155 works has been explained in our previous publication (Zhou *et al.*, 2016).

156 (3) Then the filtered intensity I_f^k of kth pixel is defined as:

$$I_f^k = \begin{cases} 0, & \text{when } I_r^k \leq I_t \\ I_r^k - I_t & \text{when } I_r^k > I_t \end{cases}$$

157   33* MERGEFORMAT ()

158 Afterwards, the averaged filtered intensity I_F of ith Laue pattern is obtained by
159 averaging the filtered intensity of all the pixels in the Laue pattern:

$$I_F = \frac{\sum\limits_{k=1}^{n \times m} I_f^k}{n \times m}$$

160   44* MERGEFORMAT ()

161   (4) Finally, the average recorded intensity I_R and averaged filtered intensity

162 I_F of all the Laue patterns are output as a *.txt file, which can be imported into

163 XtalCAMP and visualized ~~by the~~as a 2D map plot. The detailed import and plot

164 operations are introduced in Section 3.2 and 3.3, respectively. Here an example

165 is given to demonstrate how the microstructure features are studied from the

166 maps of the average recorded and filtered intensities (Fig. 2).

167   ~~The lower-left corner of~~ Fig. 2b shows the averaged filtered intensity map of

168 the Ni-based superalloy specimen. Due to the enrichment of heavy elements and

169 sharp diffraction peaks, MC-type carbides (M = W, Ta, Ti) in the substrate and

170 the HAZ give stronger intensity signals. Besides, some boundary features, which

171 are identified as low angle grain boundaries (LAGBs) in section 3.5, are observed

172 in the substrate as darker contrast, because of the peak splitting of the LPs

173 collected in these regions. As for the completely recrystallized area in the heat

174 affected zone (HAZ), the crystal orientation (and thus Laue peak indices and

175 intensity) becomes significantly different from the substrate and the cladding

176 layers~~, and thus the Laue peak indices and intensity also in remarkable contrast~~,

177 resulting through contrast in the clear visualization of high angle grain

178 boundaries (HAGBs). The non-uniform contrast in the cladding layers is

179 attributed to the local orientation gradient and microstructural defects. ~~It is~~

180 ~~noticed~~The ~~that the~~ contrast of both images can be adjusted by setting the range

181 (minimum and maximum) of the grey scale values ~~with proper values~~.
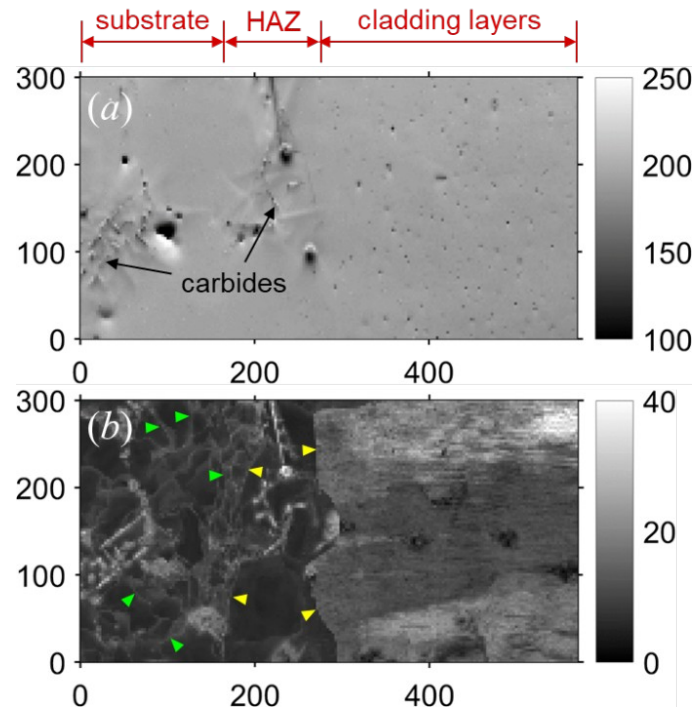
Figure 2 The diffraction intensity maps collected before Laue pattern indexation. (*a*) Average recorded intensity map; (*b*) Average filtered intensity map is obtained by a default filtered factor 4. The LAGBs and HAGBs are denoted by green and yellow triangles, respectively.

3.2. Data input

The file input function is ~~realized~~ achieved on the main window of XtalCAMP, as displayed in Fig. 3. The input data can be the μXRD results, diffraction intensity analysis output, and other ASCII files such as fluorescence data which are usually collected when μXRD experiments are performed. The μXRD results are the most frequently used on XtalCAMP so we will take it as the example. They can be in either text~~the~~ *.txt format of the output matrix from the Laue pattern indexation software packages or the binary .seq file generated specifically by XMAS after automatically processing the thousands of Laue patterns collected in raster scan mode. After loading either format through "File" menu or right-click context menu, a table ~~shows up~~appears on the screen with the same number of rows as ~~the amount~~ of the LPs. Each row is a 156-column entry, including scan spot coordinates, pattern number, diffraction geometry parameters, orientation matrix values, strain/stress tensor components, equivalent strain/stress, average peak width, and so on, which then allows the construction of 2D maps ~~denoting~~ of the distribution of a certain microstructural feature.

7

204
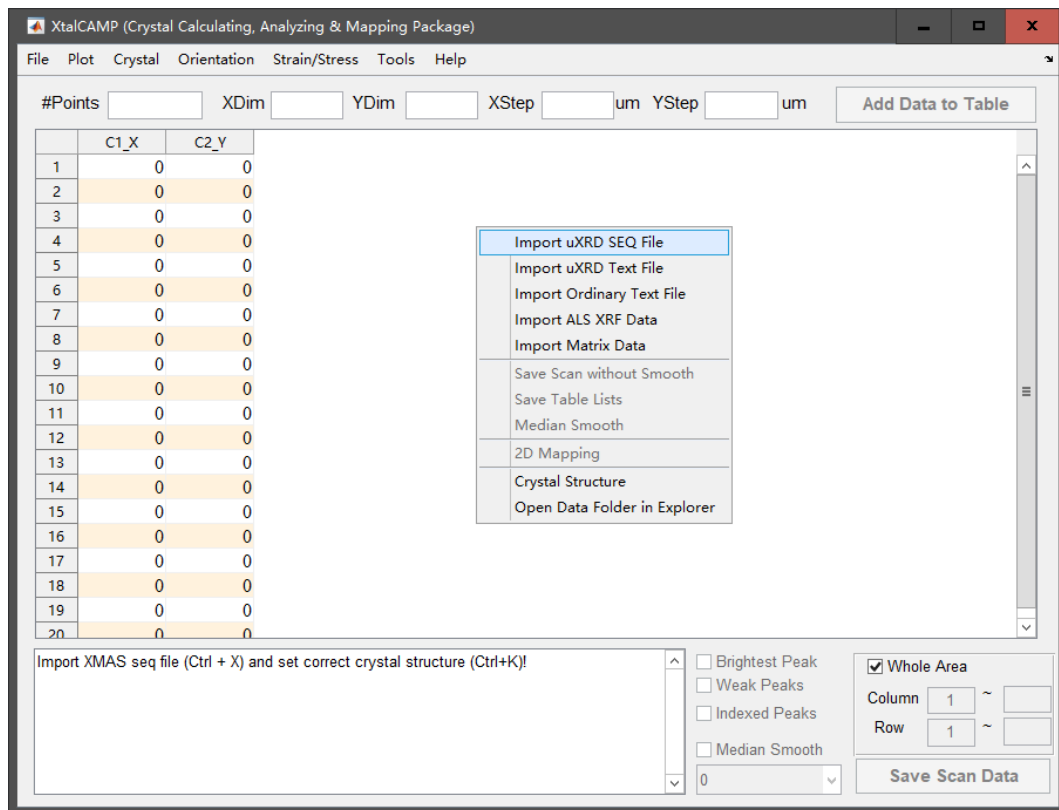
Figure 3 Main window of XtalCAMP with showing right-click options.

3.3. 2D color-coded mapping

206

207 As shown in Fig. 2, the X- and Y-coordinates of each scanning position are
208 automatically calculated according to the scanning stage positions shown in the
209 4th and 5th columns and by default displayed in the first two columns when the
210 data are loaded into XtalCAMP, and then a certain aspect of microstructure
211 characters at the location of rectangular grid sites can be visualized by plotting
212 the 2D color-coded (including the grey scale) map using the corresponding
213 column entry. On the 2D color-coded mapping interface, ~~plentiful~~ many options
214 are available to self-define the map appearance, such as ~~more than 40 kinds of~~
215 color styles, ~~alterable~~ color range, not-indexed pixels visualized in different color
216 from the colorbar, filter selections for data colored in the map, and axis label
217 settings, etc. Moreover, data cursor is designed to read the pixel value from the
218 map.

219 As shown in Fig. 4, the average peak width, which is the averaged FWHM of
220 all Laue peaks indexed in a single Laue pattern, is taken as an example. As the
221 peak width reflects the local dislocation concentration, the inhomogeneous
222 distribution indicates a relatively larger population of dislocations stored in the
223 cladding layers, in spite of the ~~disappeared~~ disappearance of dendrite structure

8

224 after solution heat treatment.
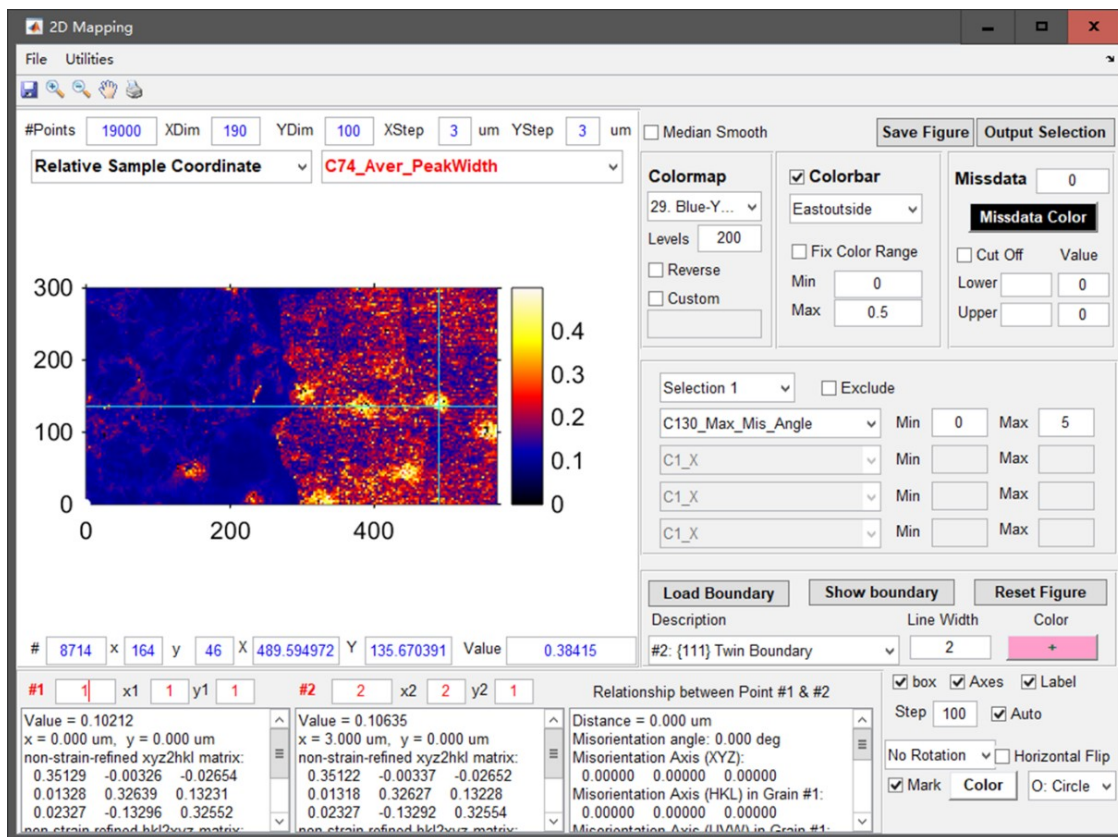
Figure 4 Snapshot of the 2D color-coded mapping interface.

3.4. Crystal selection

228   As no crystal information is contained in the *.seq file or other *.txt files, one
229 needs to pre-set the crystal structure for the crystal orientation/misorientation
230 analyis. In this case, one can access ~~to~~ the "Crystal" menu in the main window
231 (Fig. 3) and select the correct crystal file via the window shown in Fig. 5.
232 XtalCAMP supports both the standard crystallographic information file (*.cif) and
233 the crystal file (*.cri) defined by XMAS, from which the lattice and basis
234 information can be obtained. Both format can be converted to each other using
235 XtalCAMP. Once a certain crystal structure is selected, the space group and point
236 group annotations are displayed and the crystal symmetry is represented by the
237 stereographic projection of (001) pole center in the lower-right corner of Fig. 5.
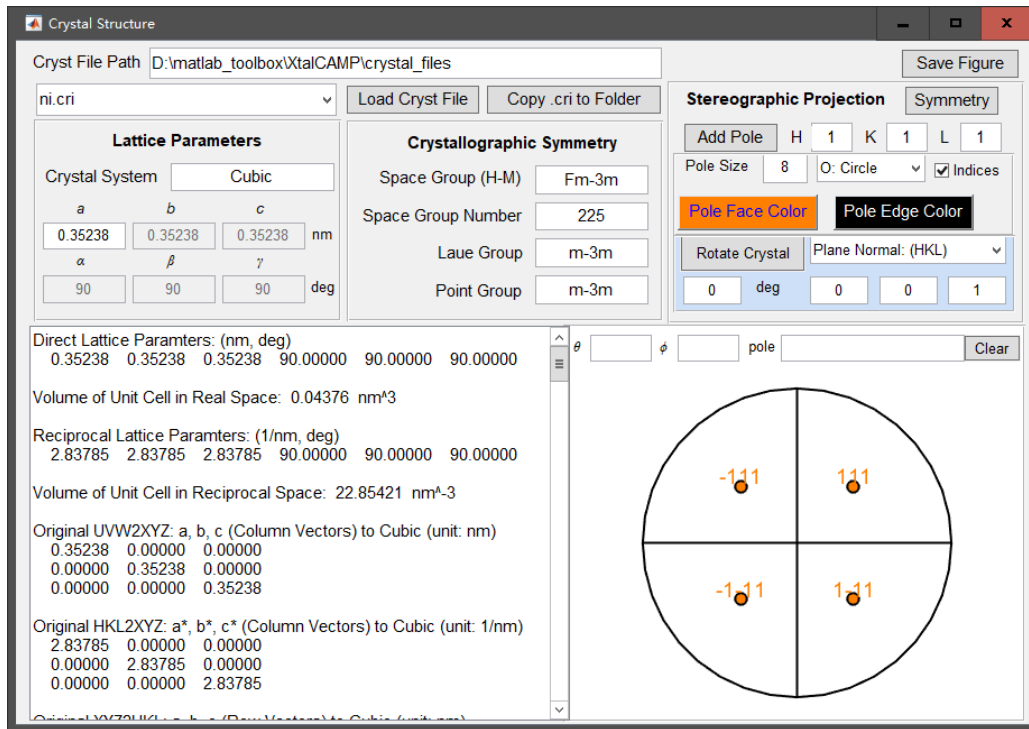
Figure 5 Crystal structure selection interface of XtalCAMP.

For crystallographic calculations (e.g. the angle between two crystal vectors) in a certain (cubic or non-cubic) crystal structure, it is convenient to ~~build up~~define a Cartesian coordinate system $\mathbf{a^o b^o c^o}$, in which $\mathbf{a^o}$, $\mathbf{b^o}$, $\mathbf{c^o}$ are unit vectors perpendicular to each other and adherent to the original crystal lattice coordinate system **abc**. Based on the common definition, the relationship between the two coordinates follows (Matthies *et al.*, 1988):

$$\mathbf{c^o} \parallel \mathbf{c}, \ \mathbf{b^o} \parallel \mathbf{c} \times \mathbf{a}, \ \mathbf{a^o} \parallel \mathbf{b^o} \times \mathbf{c^o} \qquad 55\backslash* \text{ MERGEFORMAT ()}$$

where the × denotes the cross production of two vectors. Therefore, there exists a coordinate transformation matrix ***L (Liu & Liu, 2012)***:

$$\mathbf{L} = \begin{bmatrix} a\sin\beta & b(\cos\gamma - \cos\alpha\cos\beta)/\sin\beta & 0 \\ 0 & b\sqrt{1 - \cos^2\alpha - \cos^2\beta - \cos^2\gamma + 2\cos\alpha\cos\beta\cos\gamma}/\sin\beta & 0 \\ a\cos\beta & b\cos\alpha & c \end{bmatrix} \qquad 66\backslash*$$

MERGEFORMAT ()

where a, b, c, α, β and γ are lattice parameters. It is apparent that the coordinates of lattice vectors **a**, **b**, **c** ~~are~~ correspond~~ing~~ to the columns of ***L***. Similarly, the rows of $\mathbf{L}^{-1}$ (inverse matrix of ***L***) ~~denote~~ are the coordinates of lattice vectors **a***, **b***, **c*** in reciprocal space~~, respectively~~. Therefore, the arbitrary indices of a crystal direction or plane in the coordinate system **abc** can

256   be readily converted into the coordinate system **a°b°c°** by using **L** matrix, and

257   vice versa, where the conversion equations can be found in ref (He & Jonas,

258   2007). Moreover, the determinants of **L** and **L**$^{-1}$ represent the volumes of unit cell

259   in real and reciprocal spaces, respectively. As shown in Fig. 5, **L** and **L**$^{-1}$ matrices

260   and other crystal information are displayed in the text box on the lower-left

261   corner.

262   **3.5. Orientation & misorientation analysis**

263   In XMAS *.seq file, the crystal orientation is represented by the ***xyz2hkl***

264   matrix, and its transpose matrix is denoted as **G**, which describes the rigid

265   rotation from the Cartesian coordinate system **a°b°c°** to the specimen coordinate

266   system **xyz** by a rotational operation **R**:

$$G = xyz2hkl^{\top} = RL = \begin{vmatrix} a_x & b_x & c_x \\ a_y & b_y & c_y \\ a_z & b_z & c_z \end{vmatrix}$$

267   ,   77* MERGEFORMAT ()

268   where the elements of **G** matrix represent the projections of lattice vectors **a**, **b**,

269   **c** on the **x**, **y** and **z** axes in the specimen coordinate system. The , and the **R**

270   matrix is a pure rotation matrix, which is equivalent to a set of 3 Euler angles

271   widely adopted in the electron backscatter diffraction (EBSD) software. Similar to

272   transformation matrix **L**, the vectors and Miller indices in coordinate system **abc**

273   can be converted into coordinate system **xyz** by using **G** matrix, and vice versa.

274   The misorientation matrix **M** between two crystal orientations **G**$_1$ and **G**$_2$ is

275   derived as

$$M = G_1 G_2^{-1} = R_1 L L^{-1} R_2^{-1} = R_1 R_2^{-1}$$

276   ,   88* MERGEFORMAT ()

277   where **R**$_1$ and **R**$_2$ are the corresponding rotation matrix of **G**$_1$ and **G**$_2$, respectively.

278   The misorientation matrix **M** is also a rotation matrix, which can be represented

279   as a misorientation angle–axis pair. By checking the misorientation between

280   adjacent scan spots, the boundary configurations, such as LAGB, twin boundary

281   (TB) and HAGB, in the scan area can be identified.

282   In XtalCAMP, the boundary configurations are identified by calculating the

283   misorientation angle–axis pair between the current spot P with its right neighbor

284   P_r as well as {θ_u, $\mathbf{v}_u$} between P and its upper neighbor P_u, respectively and

285   sequentially (Fig. 6a). It is explained below to demonstrate theThe procedure on

286   how the boundaries are characterized (as schematically illustrated by Fig. 6b) is

287   explained below:

288   (1) A LAGB is formed if the misorientation angle θ_r is smaller than a threshold
289   angle ω_g (user-defined ~~while~~ but commonly set as 15°), while the lower bound of
290   θ_r lacks rigorous definition and is usually dependent on the angular resolution.
291   For μXRD technique, the lower bound of θ_r can be set as 0.1°, which is 100 times
292   larger than its angle resolution.

293   (2) If the misorientation angle θ_r is larger than ω_g, the boundary is
294   characterized as a HAGB, but in many cases it is of curiosity whether it is a
295   special boundary, such as TB, or an ordinary HAGB. We have reported a look-up
296   table based approach to ~~realize~~ achieve this function (Li *et al.*, 2015). Firstly, a
297   look-up table which lists all the misorientation angle-axis pairs {θ_t, $\mathbf{v}_t$} is
298   established considering the given twin low (either plane or twin axis/angle) and
299   the rotational symmetry operations associated with the selected crystal
300   structure. Then the boundary is identified as a TB if the measured misorientation
301   meets the following two conditions simultaneously:

302    $$\left|\theta_r - \theta_t\right| < \omega_{t1} \text{ and } \theta_v < \omega_{t2},$$ 99* MERGEFORMAT ()

303   where ω_{t1} and ω_{t2} are user defined threshold angles ~~compromising~~ taking into
304   account the inherent uncertainties of orientation measurement and plastic
305   deformation effect, and θ_v is the angle between $\mathbf{v}_r$ and $\mathbf{v}_t$. Otherwise, if θ_r is larger
306   than ω_g and the conditions in equation Error: Reference source not found is not
307   satisfied, the boundary is identified as a HAGB.

308   (3) The same analysis procedure is repeated to check the boundary between
309   P and P_u.

310   By extending the process to the ~~whole scan spots~~ entire scan, the measured
311   misorientation angle–axis pairs and boundary information are output as two *.txt
312   files.
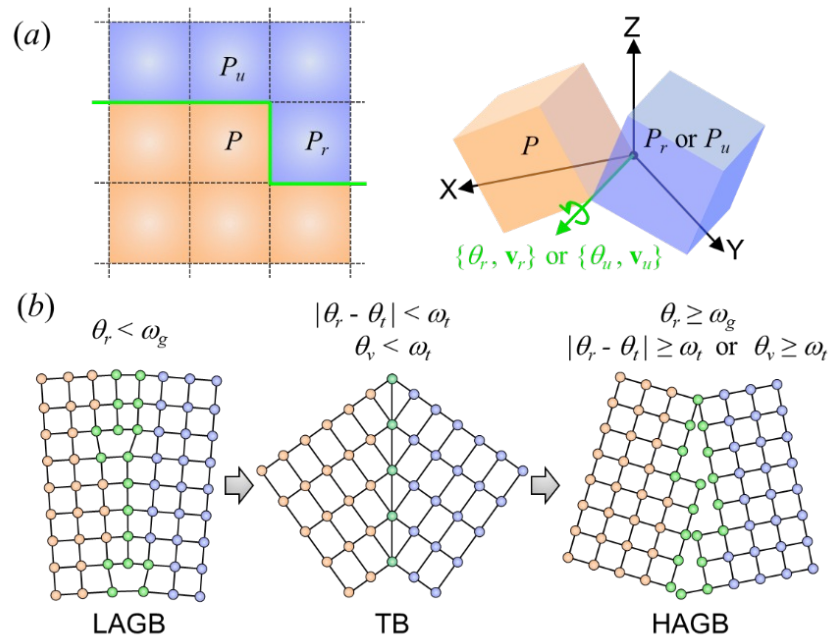
Figure 6 Schematic illustration the grain boundary characterization algorithm. (*a*) Grain boundary determination strategy; (*b*) Schematic showing the LAGB, TB and HAGB.

Here we also use the 3D-printed Ni-based superalloy data as an example. After re-loading the two *.txt files into XtalCAMP after boundary identification process, RGB inverse pole figure map (without showing the program interface) and misorientation map are plotted with TBs and HAGBs superimposed in different colors. As shown in Fig. 7(*a*), HAZ grains in different colors from the substrate and cladding layers, demonstrating the occurrence of recrystallization in the HAZ after solution heat treatment due to the large stored energy ~~contributed by~~from the high density of dislocations (Chen *et al.*, 2020). It is observed in Fig. 7(*b*) that dislocation density becomes low and a {111} twin forms with the recrystallization. Besides, LAGBs in the substrate are consistent with the contrast found in the average filtered intensity map in Fig. 3(*b*), while more LAGBs with higher misorientation angles are detected in the cladding layers, consistent with previous study (Xue *et al.*, 2015).

It is convenient to read the orientation matrix using the data cursor in the 2D color-coded map. As seen in Fig. 7, by clicking the two grains next to the TB (marked by white circle and triangle in the figure, respectively), their orientation information is listed in the bottom textboxes, and the misorientation between them is automatically calculated and shown in the third textbox, which is close to $[60°,[1\bar{1}1]]$, ~~elucidating~~ validating ~~our~~the validity ~~of our~~ TB identification algorithm. The {111} twin relationship can be further confirmed from the {111}

336   pole figure, which is implemented on the interface shown in Fig. 8. The 111 poles

337   of these two orientation are displayed in red and blue, respectively. The

338   overlapped $1\bar{1}1$ poles of the two grains ~~manifest~~ show that they share the same

339   $(1\bar{1}1)$ plane, which serves as the mirror plane between the twin and parent

340   domains.
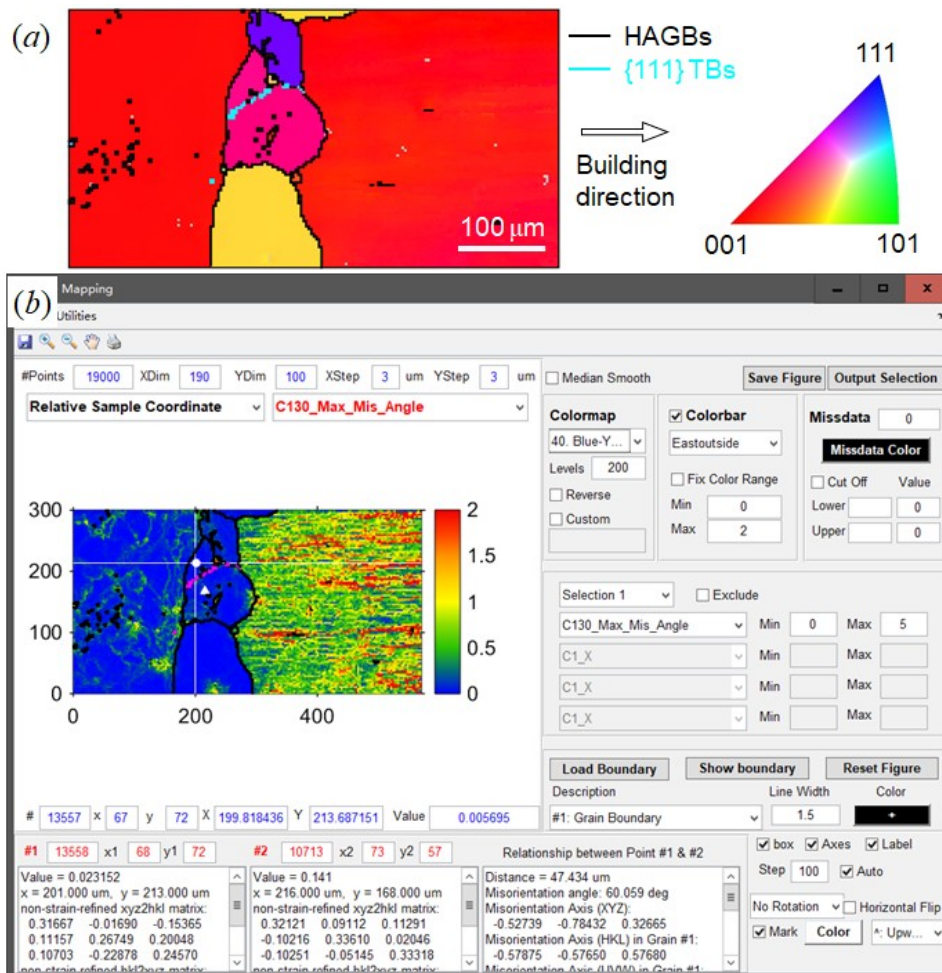
341

342   **Figure 7** Orientation and misorientation map obtained by XtalCAMP. (*a*) RGB inverse pole

343   figure map along building direction, which is rotated by 90° counter-clockwise. (*b*) 2D

344   color-coded mapping interface showing HAGBs (dark lines) and {111} TBs (pink lines)

345   superimposed on the misorientation angle map.

346
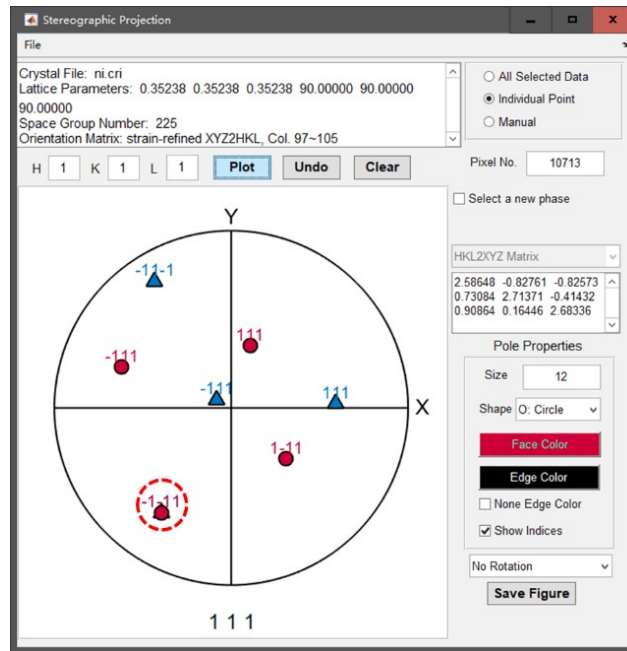
Figure 8 {111} stereographic projection of the two scan spots marked in Figure 7(*b*).
The overlapped poles are marked by the red circle.

3.6. Strain/stress analysis

For polychromatic X-ray Laue diffraction, the precise wavelength of each peak is unknown and the volumetric change of unit cell is thus indeterminable. However, the lattice distortion can be detected based on the hypothesis of constant volume of unit cell, and thus the deviatoric strain tensor ε_{ij} (3 × 3) can be measured accurately from the slight shift of Laue peak position relative to the unstrained crystal after crystal orientation is determined. ~~By knowing the~~If the stiffness ~~tensor~~ (6 × 6) tensor is known, the deviatoric stress tensor can be further calculated according to the generalized Hooke's law. The deviatoric strain/stress tensor components are contained in the output from the μXRD data processing software file and can be visualized by aforementioned 2D color-coded mapping interface.

With respect to a strained/stressed crystal, there are three mutually perpendicular planes where the shear strain/stress components are 0 but only normal strain/stress components exist. The three normal strains/stresses are termed principal strains/stresses, and the corresponding strain/stress directions are normal to these three principal planes. Under the "Strain/Stress" menu in the main window of XtalCAMP (Fig. 3), the functionality to calculate the principal strains/stresses and their directions are stored as a *.txt file, which can also be re-loaded into XtalCAMP. The magnitudes and directions of principal strains of

369   the 2nd rank strain tensors, expressed by symmetric 3 × 3 matrices, can be

370   obtained by calculating the eigenvalues and eigenvectors (Noyan & Cohen,

371   2013):

$$\boldsymbol{\varepsilon_p} = \begin{vmatrix} \varepsilon_{p1} & 0 & 0 \\ 0 & \varepsilon_{p2} & 0 \\ 0 & 0 & \varepsilon_{p3} \end{vmatrix} = \boldsymbol{T}^{\top}\boldsymbol{\varepsilon_{ij}}\boldsymbol{T}$$

372   ,   1010* MERGEFORMAT ()

373   where $\boldsymbol{\varepsilon_p}$ represents the principal strain tensor, ε_{p1}, ε_{p2} and ε_{p3} the three principal

374   strains in ascending order, $\boldsymbol{T}$ the rotation matrix composed of 3 column

375   eigenvectors, and $\boldsymbol{\varepsilon_{ij}}$ the deviatoric strain tensor. In the case of deviatoric strain

376   tensor, the summation of ε_{p1}, ε_{p2} and ε_{p3} (trace of $\boldsymbol{\varepsilon_p}$) is 0, which means ε_{p1} is

377   always compressive while ε_{p3} is always tensile (except <u>when </u>all components are

378   0). This method and conclusion are valid for stresses as well.

379   In order to show the magnitude and direction of principal strain

380   simultaneously, the superimposition of strain direction projection on the 2D

381   color-coded principal strain map is adopted, as seen in Fig. 9(*a*). As schematically

382   displayed in Fig. 9(*b*), for the projection vector $\mathbf{v_{xy}}$ of an arbitrary strain direction

383    $\mathbf{v}$, the length of $\mathbf{v_{xy}}$ can reflect the magnitude of *z*-component of $\mathbf{v}$. For an

384   overview of the strain direction distribution, the $\mathbf{v_{xy}}$ of every n^{th} (*n* is a user-

385   defined viable which is 8 in this example) scan spot is denoted by the arrow. This

386   approach has been successfully applied to explain the residual strain distribution

387   in alloys and minerals (Li *et al.*, 2015; Chen *et al.*, 2016).

388   Additionally, strain ellipsoid is used to demonstrate the magnitude and

389   orientation of the strain field. As seen in Fig. 10, $\mathbf{e_1}$, $\mathbf{e_2}$ and $\mathbf{e_3}$ denote the

390   principal strain directions and the dashed ellipses delineate the corresponding

391   principal planes. It is clear that the rotation matrix $\boldsymbol{T}$ in equation Error: Reference

392   source not found represents the rotational operation between $\mathbf{e_1e_2e_3}$ coordinates

393   to sample coordinates $\mathbf{xyz}$.
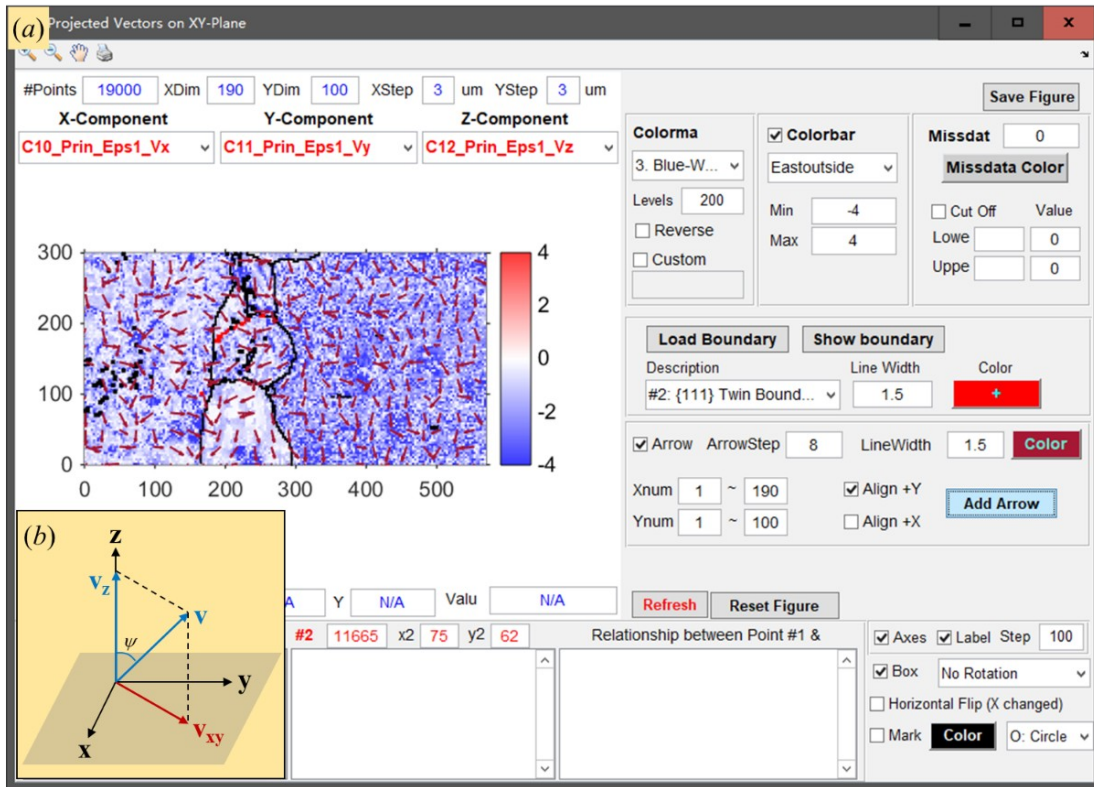
Figure 9 The principal strain visualization interface. (a) The arrows denoting the compression strain axes direction superimposed on the magnitude distribution map of principal compression strain. (b) Schematic showing an arbitrary vector projected on the **xy**-plane.
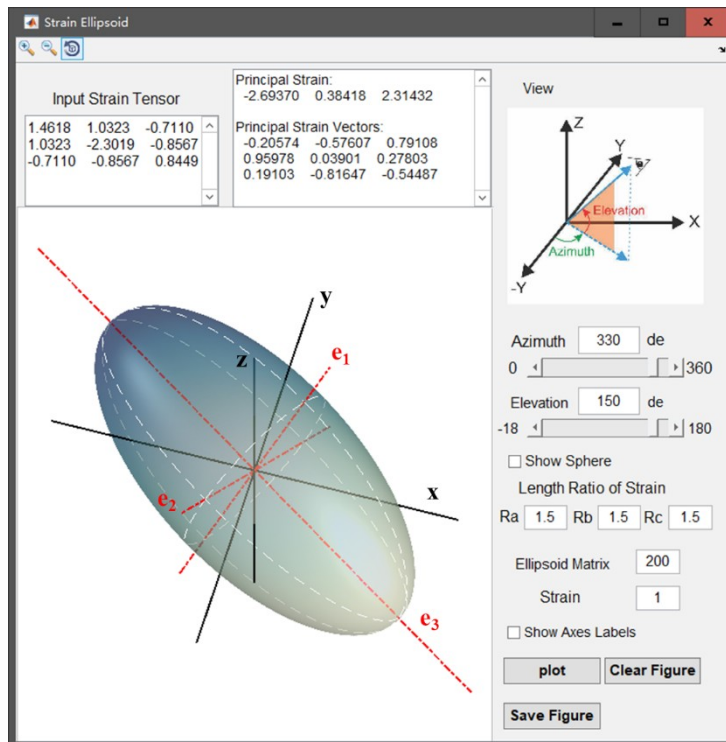
Figure 10 Strain ellipsoid interface.

17

3.7. Additional tools

In addition to the functionalities introduced above, XtalCAMP also provides ~~a batch of~~many other useful tools, which are straightforward to use, ~~as~~ and listed in Table 1.

Table 1 Additional tools in XtalCAMP.

Application	Crystallographic study	Orientation/ misorientation calculation	Data visualization
Tools	1. Equivalent directions and Miller indices; 2. Conversion between 3-digit indices to 4-digit indices in hexagonal lattice vector; 3. Angle between two vectors; 4. Conversion between plane indices and the plane normal direction; ...	1. Conversion of different orientation representations; 2. Misorientation between two **xyz2hkl** matrices by considering the rotational symmetry; 3. Construction of look-up table for twinning identification; ...	1. Contour plot; 2. 3D surface plot; 3. Inverse pole figure; 4. Misorientation profile along a line; 5. Frequency statistics of microstructural property ...

4. Conclusions and future outlook

We have described the major structure and functionalities of XtalCAMP, a GUI program dedicated to µXRD data mining and visualization. More detailed information ~~it~~ can be obtained ~~by click~~from the "Help" menu on the main interface.

XtalCAMP ~~is like to undergo continuous upgrade~~is continuously updated and more functionalities will be added based on the suggestion ~~by~~ of users. Future additions to the software will include the following two aspects:

(1) Currently, Matlab needs to be installed before running XtalCAMP. To extend its application, executable files for Windows and Mac OS systems will be developed. After achieving this, only MATLAB Runtime ~~is~~ will be required, which can be downloaded from the website (https://mathworks.com/products/compiler/matlab-runtime.html) free of charge.

(2) The µXRD technique has been merging with other advanced crystals/materials characterization techniques such as EBSD and high resolution powder diffraction, µXRD orientation measurements can be transformed into the data format compatible with EBSD data analysis software such as MTEX toolbox (Bachmann *et al.*, 2010) and other

18

| 424 | crystallographic analysis programs such as BEARTEX (Wenk *et al.*, 1998). |
| 425 | The data formation conversion functionality will be introduced in |
| 426 | XtalCAMP and extend μXRD techniques to more users. |

427

428

429 Appendix A. Sample preparation and μXRD experiment.

430 The thin-wall Ni-based superalloy sample was 3D printed using an in-house
431 developed co-axial laser cladding apparatus equipped with a 1 kW Nd:YAG laser
432 source (Do *et al.*, 2013). The substrate was cut from a directionally solidified Ni-
433 based superalloy DZ125L ingot. The DZ125L powders, ~~in the diameter~~with
434 particle diameters ranging from 40 μm to 120 μm, were used as the feedstock
435 and deposited on the (001) plane of the substrate with a fixed laser power of 180
436 W and a scan rate of 10 mm/s protected with Ar atmosphere. The Ar gas carried
437 powders were injected into the melt pool at a feeding rate of ~9 mm^3/s and the
438 layer thickness was controlled about 100 μm. After post-processing solution heat
439 treatment at 1240 °C for 2 h, a slice in the thickness of ~1.5 mm was cut
440 longitudinally and investigated under the scanning electron microscopy (SEM) in
441 backscattered electron (BSE) mode (Fig. S1) after mechanical grinding and
442 electro-polishing.

443 The solutionized sample was then further examined with the synchrotron
444 Laue μXRD experiment on beamline 12.3.2 at the Advanced Light Source in
445 Lawrence Berkeley National Laboratory (California, USA). The sample was
446 mounted 90° rotated around the surface normal with respect to the SEM image
447 on a high-precision XY-stage (so that the building direction is towards right), with
448 a 45° incline angle between the sample surface normal and incident X-ray beam.
449 By using the focused polychromatic X-ray beam in size of ~1 μm with an energy
450 bandpass between 5 and 24 keV, a total number of 19000 Laue patterns were
451 collected using a 2D detector (Pilatus 1M, 1043 × 981 in pixels) from an area of
452 570 × 300 μm^2, which covered the substrate, HAZ, and cladding layers, with 3
453 μm step size on the sample surface. Subsequently, all the Laue patterns were
454 sequentially indexed by XMAS software taking advantage of the newly developed
455 peak position comparison indexing algorithm.

456
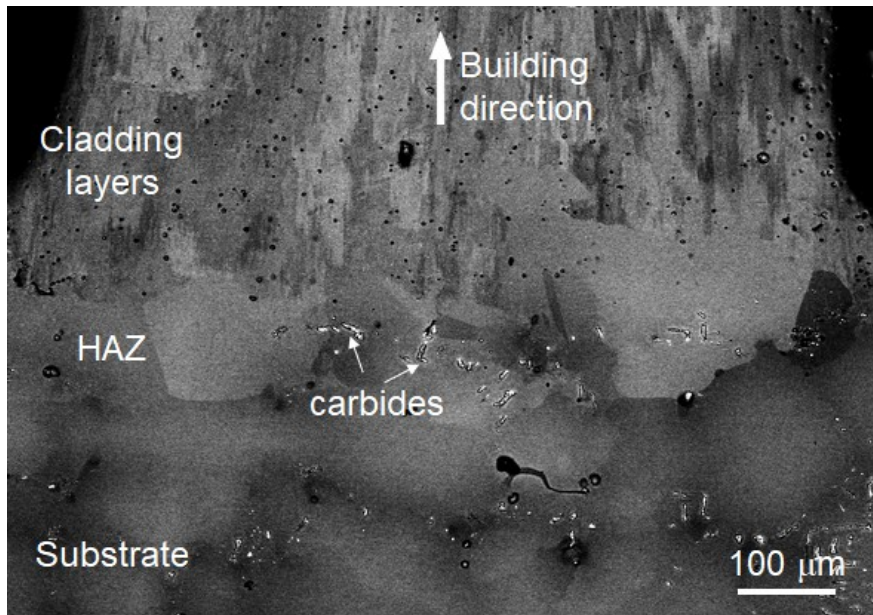
Figure S1 BSE SEM investigation on the laser 3D-printed Ni-based superalloy DZ125L
after solution heat treatment.

457
458

References

469

470 Bachmann, F., Hielscher, R. & Schaeben, H. (2010). *Solid State Phenomena*, Vol.
471   *160*, pp. 63–68.
472 Campbell, J. W. (1995). *J. Appl. Cryst.* **28**, 228–236.
473 Chen, K., Huang, R., Li, Y., Lin, S., Zhu, W., Tamura, N., Li, J., Shan, Z.-W. & Ma, E.
474   (2020). *Adv. Mater.* 1–8.
475 Chen, K., Kunz, M., Li, Y., Zepeda-Alarcon, E., Sintubin, M. & Wenk, H. R. (2016).
476   *Geophys. Res. Lett.* **43**, 6178–6185.
477 Chen, K., Kunz, M., Tamura, N. & Wenk, H. R. (2015). *Geology*. **43**, 219–222.
478 Chen, K., Tamura, N., Kunz, M., Tu, K. N. & Lai, Y. S. (2009). *J. Appl. Phys.* **106**,

479   023502.

480   Chen, K., Tamura, N., Tang, W., Kunz, M., Chou, Y. C., Tu, K. N. & Lai, Y. S. (2010).
481   *J. Appl. Phys.* **107**, 063502.

482   Chen, X., Dejoie, C., Jiang, T., Ku, C. S. & Tamura, N. (2016). *MRS Bull.* **41**, 445–
483   453.

484   Dejoie, C., Sciau, P., Li, W., Noé, L., Mehta, A., Chen, K., Luo, H., Kunz, M.,
485   Tamura, N. & Liu, Z. (2014). *Sci. Rep.* **4**, 4941.

486   Do, X., Li, D., Zhang, A., He, B., Zhang, H. & Doan, T. (2013). *J. Laser Appl.* **25**, 2–
487   7.

488   Guo, H., Chen, K., Oh, Y., Wang, K., Dejoie, C., Syed Asif, S. A., Warren, O. L.,
489   Shan, Z. W., Wu, J. & Minor, A. M. (2011). *Nano Lett.* **11**, 3207–3213.

490   He, Y. & Jonas, J. J. (2007). *J. Appl. Cryst.* **40**, 559–569.

491   Kou, J., Chen, K. & Tamura, N. (2018). *Scr. Mater.* **143**, 49–53.

492   Kunz, M., Tamura, N., Chen, K., MacDowell, A. A., Celestre, R. S., Church, M. M.,
493   Fakra, S., Domning, E. E., Glossinger, J. M., Kirschman, J. L., Morrison, G. Y.,
494   Plate, D. W., Smith, B. V., Warwick, T., Yashchuk, V. V., Padmore, H. A. &
495   Ustundag, E. (2009). *Rev. Sci. Instrum.* **80**, 035108.

496   Li, R., Xie, Q., Wang, Y.-D., Liu, W., Wang, M., Wu, G., Li, X., Zhang, M., Lu, Z.,
497   Geng, C. & Zhu, T. (2018). *Proc. Natl. Acad. Sci. U. S. A.* **115**, 483–488.

498   Li, Y., Chen, K. & Tamura, N. (2018). *Mater. Des.* **150**, 171–181.

499   Li, Y., Qian, D., Xue, J., Wan, J., Zhang, A., Tamura, N., Song, Z. & Chen, K.
500   (2015). *Appl. Phys. Lett.* **107**, 181902.

501   Li, Y., Wan, L. & Chen, K. (2015). *J. Appl. Cryst.* **48**, 747–757.

502   Liu, H. & Liu, J. (2012). *J. Appl. Cryst.* **45**, 130–134.

503   Lupinacci, A., Chen, K., Li, Y., Kunz, M., Jiao, Z., Was, G. S., Abad, M. D., Minor, A.
504   M. & Hosemann, P. (2015). *J. Nucl. Mater.* **458**, 70–76.

505   Ma, E. Y., Cui, Y. T., Ueda, K., Tang, S., Chen, K., Tamura, N., Wu, P. M., Fujioka,
506   J., Tokura, Y. & Shen, Z. X. (2015). *Science.* **350**, 538–541.

507   Matthies, S., Wenk, H.-R. & Vinel, G. W. (1988). *J. Appl. Cryst.* **21**, 285–304.

508   Micha, J.-S. (2017). *LaueTools, Open Source Python Packages for X-Ray
509   MicroLaue Diffraction Analysis*, https://sourceforge.net/projects/lauetools/.

510   Noyan, I. C. & Cohen, J. B. (2013). *Residual stress: measurement by diffraction
511   and interpretation*, Springer.

512   Ouladdiaf, B., Archer, J., McIntyre, G. J., Hewat, A. W., Brau, D. & York, S. (2006).
513   *Phys. B Condens. Matter.* **385**–**386**, 1052–1054.

514   Soyer, A. (1996). *J. Appl. Cryst.* **29**, 509.

515 Strelcov, E., Tselev, A., Ivanov, I., Budai, J. D., Zhang, J., Tischler, J. Z.,
516   Kravchenko, I., Kalinin, S. V. & Kolmakov, A. (2012). *Nano Lett.* **12**, 6198–
517   6205.
518 Tamura, N. (2014). *Strain and Dislocation Gradients from Diffraction: Spatially-*
519   *Resolved Local Structure and Defects*, edited by R. Barabash & G. Ice, pp.
520   125–155. London: World Scientific.
521 Tischler, J. Z. LaueGo, *Https://www.Aps.Anl.Gov/Sectors-33-34/34-ID-E/34-ID-E-*
522   *Beamline-Resources/Software-Downloads*.
523 Wenk, H.-R., Matthies, S., Donovan, J. & Chateigner, D. (1998). *J. Appl. Cryst.* **31**,
524   262–269.
525 Xue, J., Zhang, A., Li, Y., Qian, D., Wan, J., Qi, B., Tamura, N., Song, Z. & Chen, K.
526   (2015). *Sci. Rep.* **5**, 14903.
527 Zhou, G., Kou, J., Li, Y., Zhu, W., Chen, K. & Tamura, N. (2018). *Quantum Beam*
528   *Sci.* **2**, 13.
529 Zhou, G., Zhu, W., Shen, H., Li, Y., Zhang, A., Tamura, N. & Chen, K. (2016). *Sci.*
530   *Rep.* **6**, 28144.
531